Journal of Energy Storage 19 (2018) 337–347

Contents lists available at ScienceDirect

Journal of Energy Storage

journal homepage: www.elsevier.com/locate/est

New insights into the electrochemical behaviour of porous carbon electrodes for supercapacitors

Dina Ibrahim Abouelamaiem[a], María José Mostazo-López[b], Guanjie He[c], Drasti Patel[a], Tobias P. Neville[a], Ivan P. Parkin[c], Dolores Lozano-Castelló[b], Emilia Morallón[d], Diego Cazorla-Amorós[b], Ana Belen Jorge[e], Rongfang Wang[f], Shan Ji[g], Maria-Magdalena Titirici[e], Paul R. Shearing[a], Daniel J.L. Brett[a,*]

[a] Electrochemical Innovation Lab, Department of Chemical Engineering, University College London, London, WC1E 7JE, UK
[b] Departamento de Química Inorgánica e Instituto Universitario de Materiales, Universidad de Alicante, Apartado 99, E-03080 Alicante, Spain
[c] Christopher Ingold Laboratory, Department of Chemistry, University College London, London, WC1H 0AJ, UK
[d] Departamento de Química Física e Instituto Universitario de Materiales, Universidad de Alicante, Apartado 99, E-03080 Alicante, Spain
[e] Materials Research Institute, School of Engineering and Materials Science, Queen Mary University of London, London, E1 4NS, UK
[f] Qingdao University of Science and Technology, Institute of Chemical Engineering, 266000 Qingdao, China
[g] College of Biological, Chemical Sciences and Engineering, Jiaxing University, 314001, China

ARTICLE INFO

Keywords:
Activated carbons
Extreme potentials
in situ Raman spectra
Porous morphology
Supercapacitor

ABSTRACT

Activated carbons, with different surface chemistry and porous textures, were used to study the mechanism of electrochemical hydrogen and oxygen evolution in supercapacitor devices. Cellulose precursor materials were activated with different potassium hydroxide (KOH) ratios, and the electrochemical behaviour was studied in 6 M KOH electrolyte. *In situ* Raman spectra were collected to obtain the structural changes of the activated carbons under severe electrochemical oxidation and reduction conditions, and the obtained data were correlated to the cyclic voltammograms obtained at high anodic and cathodic potentials. Carbon-hydrogen bonds were detected for the materials activated at high KOH ratios, which form reversibly under cathodic conditions. The influence of the specific surface area, narrow microporosity and functional groups in the carbon electrodes on their chemical stability and hydrogen capture mechanism in supercapacitor applications has been revealed.

1. Introduction

Porous carbons have been extensively exploited in electrochemical applications including gas storage and separation, catalyst supports and energy conversion and storage electrodes [1,2]. Carbon is the most versatile element on earth with the highest catenation power and when combined with other atoms, leads to materials with unique properties including high specific surface area, tuneable chemical structure/functional groups, electronic and ionic conductivity, lightweight and more. Due to all these unique features, carbon materials are ideal candidates for energy conversion and storage devices [3]. Activated carbons, a special class of amorphous microporous carbons, have been intensively used as supercapacitor electrode materials, as well as to store hydrogen by controlling the resulting microporosity and surface chemistry [4–8]. The role of the factors above and their importance in the electrochemical hydrogen storage mechanism have been previously discussed [9–11]. Nanostructured carbons have gained increasing interest as a promising alternative for electrochemical energy storage systems in aqueous media; however, the fine-tuning of the pore structure and surface functionality is yet to be fully addressed [10]. It was found that the hydrogen uptake increases with narrow microporosity and an increase in unsaturated carbon atoms, i.e. low content in surface oxygen functionalities, favours electrochemical storage of hydrogen *via* the electroreduction of water in basic media [12]. Ultra-microporosity also plays an important role in hydrogen uptake and storage, whereby a hierarchical porous structure consisting of meso- and macro-pores can provide the mass transport channels to the smaller pores, which therefore provide excellent capacity retention and promising features for electrochemical hydrogen storage applications [13]. In addition, the presence of functional groups has previously been proven to affect the hydrogen adsorption mechanism negatively, whereby the trapping of the nascent hydrogen atoms decreases upon increasing the amount of surface oxygen groups. It was suggested that active sites that are saturated with oxygen groups cannot contribute to the hydrogen trapping

* Corresponding author.
E-mail address: d.brett@ucl.ac.uk (D.J.L. Brett).

https://doi.org/10.1016/j.est.2018.08.014
Received 27 June 2018; Received in revised form 17 August 2018; Accepted 18 August 2018

mechanism, given that the porosity is kept constant [12].

Levya-Garcia et al. reported that carbon-hydrogen bonds form reversibly when using KOH¯activated carbon materials from anthracite and commercial activated carbons in different aqueous media under cathodic conditions [14]. *In situ* Raman spectroscopy and surface chemistry characterization *via* temperature programmed desorption (TPD) technique were employed in this study and it was found that the surface functionality and porous texture play a major role in determining the electrochemical hydrogen storage process [12]. The efficient process of hydrogen storage in activated carbons has proven to be more efficient than in carbon nanotubes or other methods, including pressure and cryogenic conditions, due to the easy penetration of nascent hydrogen produced in the electrolyte into the porous carbon network [15,16]. However, a direct correlation between the structural properties, presence of functional groups, pore size distribution and wettability of nanocarbons and reversible hydrogen chemisorption and storage has not yet been identified [1]. Hence, there is a vital need to better understand the hydrogen/energy storage in supercapacitor devices in order to improve their performance in terms of reversibility of the porous electrode material.

Carbon/carbon supercapacitors belong to the class of electrical double-layer capacitors (EDLCs), where energy is stored *via* charge separation at the electrode/electrolyte interface [17]. The charge storage mechanism excludes any pseudocapacitive behaviour, and the electrolyte ions are electrostatically and reversibly adsorbed in the double-layer of the porous networks of the carbon electrodes. However, in the case of surface functionalities, Faradaic processes may arise that comprise of reversible reactions between the functional groups at the accessible electrode surface and electrolyte ions. Hence, the pore size distribution, porosity and functional groups content can be tuned to optimize the electrochemical performance of supercapacitors. Nanostructured electrodes have gained increasing popularity as the manipulation of narrow microporosity and surface functional groups leads to an enhancement in the gravimetric capacitance, as well as self-discharge mechanism (the relaxation of potentials across the elements of the porous electrodes) in supercapacitors, hence increasing the energy and power densities of carbon materials [18,19]. The non-ideal polarization of carbon surfaces, due to surface oxidation reactions and possible intercalation processes, specifically upon cathodic polarization, makes fundamental understanding of the electrochemical processes occurring very challenging [18]. The behaviour of EDLCs is surface specific, whereby adsorption interactions between oxygen species on the carbon surface and electrolyte ions occur. The identification of surface functionalities on carbon surfaces and their effect on potential-of-zero-charge, the contact angle between electrode/electrolyte interface and wettability of electrode materials, have been studied previously via *in situ* X-ray photoelectron spectroscopy (XPS), Raman spectroscopy and Fourier transform infrared (FTIR) techniques [20–23]. However, and to the authors' best knowledge, this is the first time that *in situ* Raman spectroscopy has been employed to study the extreme anodic and cathodic conditions that activated porous carbon electrodes can endure for supercapacitor applications, which is correlated to the porous structure and oxygen content.

This work allows the investigation of the effect of different pores sizes and surface functional groups at the highest possible potentials applied prior to undesirable gas evolution at anodic and cathodic conditions. The crucial relationship between the electrode structure and the applied potentials would grant the application of wider potential limits in aqueous systems and therefore achieving better supercapacitor electrochemical performance in terms of energy and power delivery. This study opens a platform to i) understand the behaviour of different carbon electrodes at extreme conditions and ii) correlate the surface and morphological effects of different porous structures to the electrochemistry in order to avoid the electro-reduction and/or electro-oxidation processes.

2. Experimental

2.1. Carbon activation

Chemical activation of softwood Kraft cellulosic pulp (UPM-Kymmene Corporation, Finland) with different KOH loadings was conducted under a nitrogen atmosphere at a flow rate of 1 L min^{-1} heating ramp of 20 °C min^{-1} up to 850 °C with a dwell time of 1 h, as reported elsewhere [24]. Briefly, the cellulose of 500 g m^{-2} areal density was soaked in different concentrations of KOH solutions and dried in a vacuum oven overnight prior to the carbonization process. The KOH / cellulose weight ratios used were: 0.005:1, 0.01:1, 0.1:1, 0.5:1, 1:1, 2:1 and 3:1. All samples are denoted as KOH $-n$, with n representing the weight ratio of KOH/cellulose.

2.2. Characterization of porous texture and surface chemistry

The surface structure of the carbonized samples was characterized with scanning electron microscopy (SEM) at 10 kV in the secondary electron imaging mode (EVO MA10, ZEISS, Germany) and transmission electron microscopy (TEM) with 200 kV accelerating voltage (JEOL, JEM-2100, UK). The porous texture of the eight samples was characterized with nitrogen adsorption-desorption isotherms at 77 K (3Flex Surface and Catalyst Characterization System, Micromeritics, USA) and carbon dioxide adsorption isotherms at 273 K (Autosorb-6, Quantachrome) that followed sample degassing at 200 °C overnight (VacPrep 061 Sample Degas System, Micrometrics, USA). The total pore volume was determined at a relative pressure (P/P_o) of 0.99, and the microporous contribution was evaluated using the non-local density functional theory (NLDFT) method to the N_2 adsorption on carbon slit pores [25,26]. Micromeritics ASAP 2010 software was used to interpret the data acquired for each sample. The ultra-micropore volume (with pore sizes < 0.7 nm) were calculated using the Dubinin-Radushkevich (DR) method at relative pressures below 0.025 from the CO_2 adsorption isotherms. The densities of the absorbed phases, N_2 and CO_2, used were 0.808 g cm^{-3} and 1.023 g cm^{-3}. Specific surface areas (SSA) were obtained by applying the Brunauer-Emmet-Teller (BET) method, calculated at relative pressure range between 0.001 and 0.2. The macropore size distribution and total macropore volume of the carbonized samples were determined using mercury intrusion porosimetry (MIP) (Poremaster, Quantachrome Instruments, USA).

The surface chemistry of the carbon materials was assessed using temperature programmed desorption (TPD) conducted in a DSC (differential scanning calorimetry)-TGA (thermogravimetric analysis) instrument (TA Instruments, SDT Q600 Simultaneous) coupled with a mass spectrometer (Thermostar, Balzers, GSD 300 T3). 5 mg of each sample were heated up to 950 °C at a heating ramp of 20 °C min^{-1} under a helium flow rate of 100 ml min^{-1}. To further analyse the surface chemistry in the different carbon materials, X-ray photoelectron spectroscopy (XPS) measurements were obtained on a K-ALPHA Surface Analysis spectrometer (Thermo Scientific) with monochromatic aluminium Kα as the excitation source. CasaXPS software was used to analyse the changes in binding energy of C_{1S} peaks corresponding to different activated carbons and provide detailed information on the surface functionalities and individual carbon peaks. The oxygen/carbon ratios were determined from the C_{1S} and O_{1S} peaks and using Shirley background subtraction.

The wettability behaviour of the various activated carbons has been determined by measuring the contact angle between water and the surface of the prepared carbon electrodes (95:5 wt.% carbon: polytetrafluoroethylene) using First Ten Angstroms (FTA) 1000 B Drop Shape Analyzer (First Ten Angstroms Inc., USA). The contact angle was measured using the software FTA32 Video 2.1.

Table 1
Porous texture and surface chemistry characterization of all activated carbon samples.

Sample	SSA ($m^2 g^{-1}$)	V(CO_2) ($cm^3 g^{-1}$)	V(N_2) ($cm^3 g^{-1}$)	Macropore Volume ($cm^{-3} g^{-1}$)	μmol CO (g^{-1})	μmol CO_2 (g^{-1})	μmol O (g^{-1})
KOH-0	11	0.23	0.008	0.02	699	292	1283
KOH-0.005	252	0.22	0.16	0.03	786	324	1435
KOH-0.01	598	0.22	0.28	0.15	836	366	1570
KOH-0.1	717	0.28	0.34	0.79	1599	990	3581
KOH-0.5	1351	0.42	0.55	1.98	1828	937	3702
KOH-1	1063	0.54	0.47	3.82	1911	976	3862
KOH-2	1579	0.6	0.59	5.24	2178	1399	4976
KOH-3	785	0.16	0.43	2.22	1633	1258	4150

2.3. Electrochemical characterization

Activated carbons were prepared as electrode pastes by mixing 95 wt. % of the synthesized carbons and 5 wt.% polytetrafluoroethylene (PTFE) binder solution (Sigma Aldrich, UK). The carbon slurry was manually pasted on nickel foam (Suzhou JSD Co. Ltd., China) acting as a current collector. All samples had a final weight of 5–6 mg of activated carbon per 1 cm^2 physical surface area. Platinum and saturated Ag/AgCl electrodes purchased from Tianjin AiDaHengSheng Technology Development Co. Ltd., China, were used as counter and reference electrodes, respectively, throughout all electrochemical measurements. Further details can be found in [24].

The resistivity of the prepared electrodes was measured using the Ecopia HMS-3000 Hall Measurement System (Four-Point-Probes, USA) after pressing all electrodes in sheets of 30 μm thickness. Three measurements were taken at different points of the samples and were averaged. Electrochemical impedance spectroscopy (EIS) measurements were conducted at open circuit potential in the frequency range 0.01 Hz - 1 MHz with alternating signal of 5 mV amplitude, to compare the charge transfer resistances and electrolyte resistances inside the pores of the different carbon electrodes.

The electrochemical performance of the three-electrode systems was also studied by cyclic voltammetry (CV) in 6 M KOH electrolyte solution using a Gamry potentiostat (Interface 1000, SciMed, UK). The electrodes were soaked for 24 h in the electrolyte solution prior to electrochemical tests. CVs were conducted at a scan rate of 5 mV s^{-1} at different potential ranges until extreme cathodic and anodic polarizations are reached, for separate samples. Galvanostatic charge-discharge (GCD) at current densities ranging between 0.5 A g^{-1} and 20 A g^{-1} were also measured in the three-electrode electrochemical system.

2.4. In situ Raman spectroscopy characterization

The activated carbon pastes were prepared by mixing the carbon powder and 60 wt. % PTFE solution in a ratio of 95:5; the slurry was then vacuum-dried at 80 °C for 2 h and soaked in 6 M KOH solution overnight. The activated carbon sample was then deposited on a glassy carbon disc of 3 mm diameter acting as the electrical contact and enveloped by a polytetrafluoroethylene (PTFE) piece. The working electrode was fitted into a spectroelectrochemical PTFE cell, covered with a quartz window to form a closed system and to separate the microscopic lens from the electrolytic solution while acquiring Raman spectra. A three-electrode system was implemented with a platinum wire as the counter electrode and saturated Ag/AgCl as the reference electrode, placed through a Luggin capillary to ensure contact with the 6 M KOH electrolyte solution. A schematic of the cell for the Raman acquisition data can be found in [27].

In situ Raman characterization was conducted using a LabRam spectrometer (Jobin-Yvon Horiba, UK) coupled with a microscope Olympus BX30 (UK). All presented spectra are deconvoluted using the Lorentz function to separate multiple components from different bands in the same spectrum [28]. All data acquired correspond to an average of four measurements with an acquisition time varying between 40 s and 100 s per measurement upon an excitation line provided by 17 mW He-Ne laser at 632.8 nm A slice of silicon (521±2 cm^{-1}) was used for the calibration of the spectrometer prior to experiments. The laser beam was focused into a 2 μm spot at the electrode surface through a 50 × long-working objective (0.5 NA). The viewing system comprised of a television camera coupled with the microscope. The resolution of the spectrometer was better than 3 cm^{-1} throughout all measurements and the detector used was a Peltier cooled charge-coupled device (1064 × 256 pixels). The confocal pinhole employed was set to 600 μm and a 600 lines mm^{-1} diffraction grating was used with an aperture slit of 200 μm. The spectra were collected at each potential once a steady-state current was reached upon applying chronoamperometry [14,29,30] by using a DropSens portable bipotentiostat/galvanostat μstat 400.

3. Results and discussion

3.1. Porous texture and surface chemistry

The porous texture and surface chemistry of all activated carbons were first characterized by SEM and TEM techniques (Figs. S1 and S2). The fibrous structure of the non-activated sample (KOH− 0) with a limited amount of micropores evolved to a more porous structure upon increasing the KOH loading. Further increase in the KOH/cellulose ratio reveals the domination of macropores in the porous networks. These results were confirmed with the sorption isotherms and MIP measurements. The total pore volume, determined by N_2 and CO_2 isotherms, and SSA values are enhanced by increasing the KOH loading until they reach a maximum in the KOH− 1 and KOH− 2 samples (Table 1); beyond which the values decrease again, as reported elsewhere [24]. The macropores contribution to the total pore volume was determined by MIP and found to increase with KOH loading. It is worth mentioning that not all peaks obtained by MIP constitute the pore volume, but might include the interparticle porosity, and hence deconvolution of the data was required [31]. The KOH activation process resulted in a hierarchical porous structure in samples KOH−0.5, KOH−1 and KOH−2 having a wide pore size distribution of micro-, meso- and macropores. The narrow micropore volume, detected by CO_2 adsorption, increased with the KOH / cellulose ratio, yet the microporous contribution to the total porosity decreased. The fraction of ultra-micropores (pores of diameter < 0.7 nm) decreased from 97% in the non-activated sample (KOH−0) to 27% with the highest activation (KOH−3). If the micropores (< 2 nm) measured by N_2 physical adsorption were taken into account in the total micropore volume value in addition to the macropore volume determined by MIP, the micropore fraction of the total porous network is observed to decrease from 97% in the KOH−0 sample to a minimum of 8% in the KOH−3 sample. Fig. S3 presents the isotherms and pore size distribution of all KOH-*n* activated and non-activated samples. All samples characterized with N_2 adsorption display a Type I isotherm [32], which is a characteristic of a microporous solid and shows a shift from a narrow microporous structure at low activation ratios, to a wider micro- and macropore size

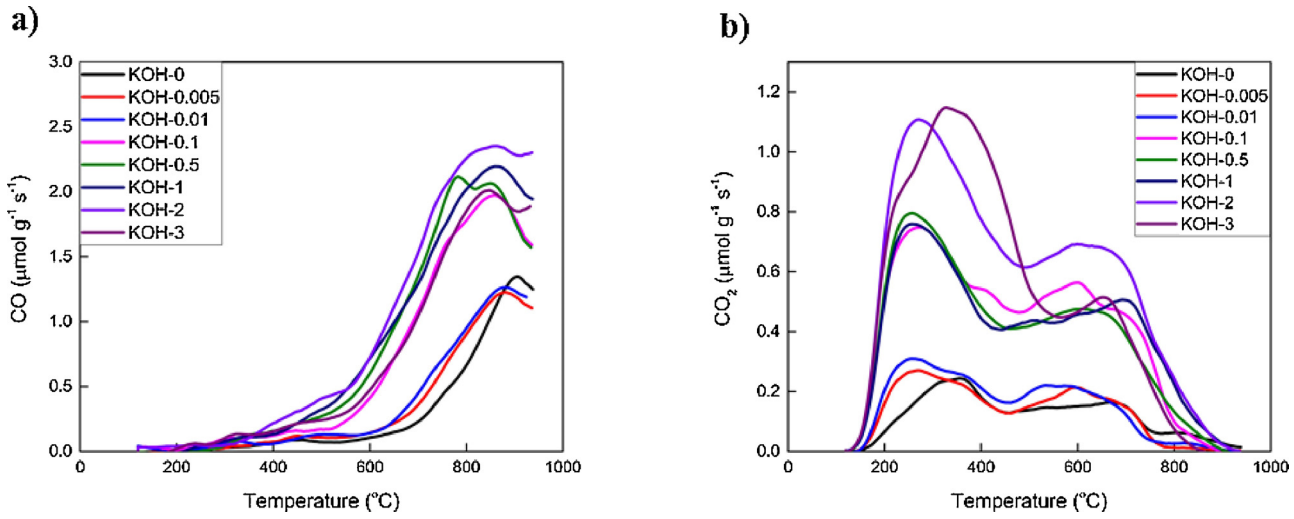

Fig. 1. TPD profiles of activated carbon materials showing the: a) CO and b) CO_2 profiles.

distribution (as detected from MIP measurements) and a hierarchical porous network at intermediate KOH loadings and finally a macroporous structure at high activation ratios.

The TPD data presents the evolution of carbon monoxide (CO) and carbon dioxide (CO_2) gases through the decomposition of oxygen surface functionalities upon heating the samples up to 950 °C (Fig. 1). CO evolves at high temperatures, mainly due to the decomposition of basic and neutral functional groups, such as phenols, carbonyls, ethers and quinones. However, the decomposition of lactones and carboxylic groups occurs at lower temperature, giving rise to the evolution of CO_2. Anhydride groups decompose to give CO and CO_2. The desorbed amounts from the TPD profiles show that the content of surface oxygen groups increases with the activation of the cellulose precursor materials with KOH until a maximum is reached at KOH − 2. The amount of total oxygen desorption can be deduced as follows:

$$\mu mol\ O\ g^{-1} = \mu mol\ CO\ g^{-1} + 2 \times \mu mol\ CO_2\ g^{-1} \quad (1)$$

The TPD profiles consist of different peaks for the CO and CO_2 profiles, which reveal the presence of different functional oxygen groups in the KOH − activated samples. Several peaks in the CO spectra show that carboxylic anhydrides are decomposed at 500 °C and carbonyl, phenol, ether and quinone groups are decomposed at higher temperatures for all samples [33,34]. In the CO_2 spectra, three peaks are detected: i) a peak at 300 °C related to the decomposition of carboxyl groups, ii) a peak at 500 °C corresponding to carboxylic anhydrides and iii) peaks beyond 500 °C related to the decomposition of lactones or CO_2 *via* secondary reactions that are boosted in porous carbon structures [35]. All samples present a diversity in oxygen functionalities on the carbon surface; however, larger amounts of CO and CO_2 desorption occur at higher KOH loadings, with the maximum reached in the KOH − 2 sample. The oxygen wt. % increased from 2.1% in KOH − 0 to a maximum of 8% in KOH − 2, decreasing again to 6.6% in KOH − 3.

XPS data of all activated and non-activated samples were investigated. Fig. 2 and S4 show the C_{1s} spectra with a broad oxygenated carbon spectrum in a binding energy (BE) range of ~ 284.1 − 288.8 eV with KOH loading. The carbon peak corresponding to the C–C, C=C and C–H bonds at a binding energy of 284.1 − 284.2 eV, exhibited the highest intensity in the non-activated sample (KOH − 0) with a small shoulder representing the carbon-oxygen bonds. The shoulder percentage increased to a maximum in KOH − 2, as indicated in Table 2. The detailed deconvoluted information of the variation in surface chemistry shows that the oxygenated carbon percentage and oxygen / carbon atomic ratio has increased with the activation. The intensities of C_{1s} signal corresponding to C − O, C = O, and O–C=O bonds show pronounced peaks at ~285.8 eV, ~287.1 eV and ~288.6 eV, respectively. They increased in relative abundance from 22.5% in KOH − 0 to 36.7% in KOH − 2, showing more oxygen surface functionalities with increased activation. The decrease in oxygen content upon further activation in KOH − 3 could be attributed to the dominant macroporous morphology and decrease in the specific surface area of the materials which also decreased the total CO and CO_2 desorption in TPD experiments. These results are confirmed with XPS data, despite the fact that XPS is not directly/qualitatively comparable with TPD, as the former provides information at the most external surface of the sample. The discrepancy in oxygen percentages between XPS and TPD techniques is because TPD analysis usually underestimates the oxygen content as some oxygen functionalities can be decomposed into water or decompose at higher temperatures than those reached by TPD, and hence are not quantified [30]. However, the trends obtained by both experiments are very similar and the peaks corresponding to different oxygen functional groups detected by TPD correspond to the intensities of C − O (ether groups), C = O (carbonyl groups) peaks and O–C=O (carboxyl groups) peaks obtained by XPS.

The increase in the oxygen content played a major role in determining the wettability of the different carbon electrodes. The water droplets in the un-activated and low-activated samples (KOH − 0, KOH − 0.005 and KOH − 0.01) stayed floated on top of the carbon pastes, showing a relatively large contact angle of more than 90°, proving the hydrophobic nature of these carbons (Fig. S5). However, the wetting behaviour of higher activated samples showed immediate dispersion/spreading of the water droplets on top of the samples and therefore their more hydrophilic nature. The contact angle increases again in KOH − 3 sample due to the decrease in the oxygen content, as shown by XPS measurements. The different wettability characteristics of the KOH-*n* activated carbons are attributed to the different extent of the amounts of polar oxygenated groups generated by the KOH activation, in addition to the variation in the porous morphology, which will be discussed in the following sections.

The amount of oxygen functional groups on the surface as determined by XPS directly correlates to the total amount of oxygen evolved in the TPD experiment (Fig. 3). The desorbed oxygen content by the TPD experiment and that analysed by XPS were compared with the microporous volume contribution (ultra-micropores and micropores determined by N_2 and CO_2 isotherms) to the samples' structure. It is evident that the oxygen desorbed at the carbon surfaces rises by at least two-fold with the activation of the carbon atoms with higher KOH concentrations (decrease in total micropore contribution); yet, there is no direct correlation between both parameters. The high values of specific surface area (high microporous content) provide sites for

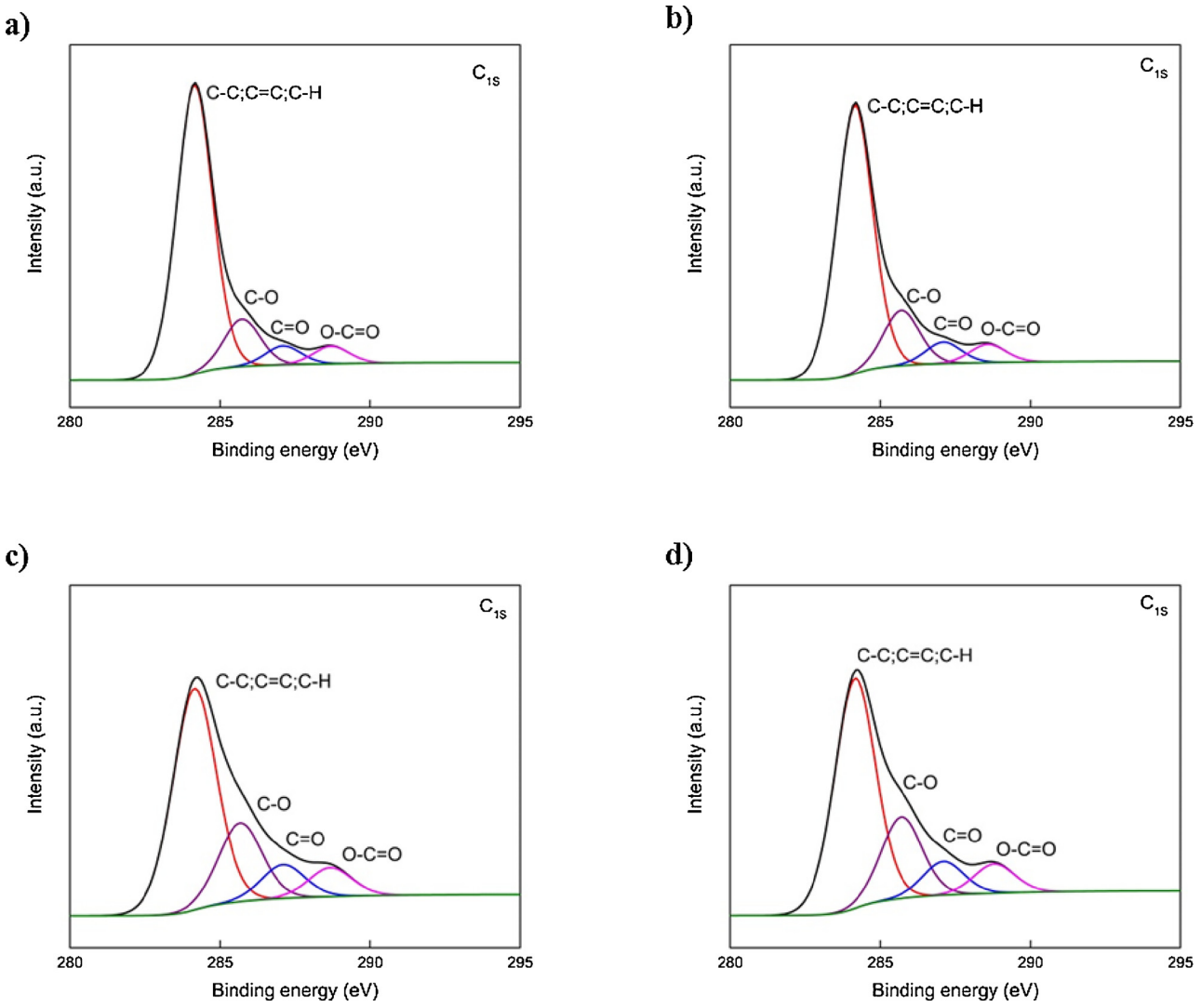

Fig. 2. C_{1S} XPS deconvolution of a) KOH − 0, b) KOH − 0.01, c) KOH − 1 and d) KOH − 2 with Shirley background subtraction (in green).

Table 2
Fitted results of percentages of oxygen to carbon content and C1S XPS data of all samples.

Sample	O:C Ratio (%)	C—C, C=C, C—H (284.1-284.2 eV)	C—O (285.7-285.9 eV)	C=O (287.1 eV)	O—C=O (288.4-288.8 eV)
KOH−0	7.78	77.6	12.6	5.1	4.7
KOH−0.005	9.6	77.0	12.7	5.6	4.7
KOH−0.01	14.1	75.5	14.6	5.4	4.5
KOH−0.1	21.11	70.3	20.6	2.7	6.4
KOH−0.5	21.01	67.9	21.1	5.9	5.1
KOH−1	18.06	65.2	21.2	7.6	6.0
KOH−2	22.7	63.3	21.5	7.8	7.4
KOH−3	13.87	71.6	16.5	6.6	5.3

oxygen functional groups; however, the samples exhibit different porous textures and surface chemistry as determined by the physical adsorption isotherms, TPD and XPS data. Hence, the total oxygen content does not rely solely on the level of activation of the precursor material, but also on the porosity, pore size distribution and surface chemistry, in which each plays a critical factor in the electrochemical performance of these materials and will be discussed in the following section.

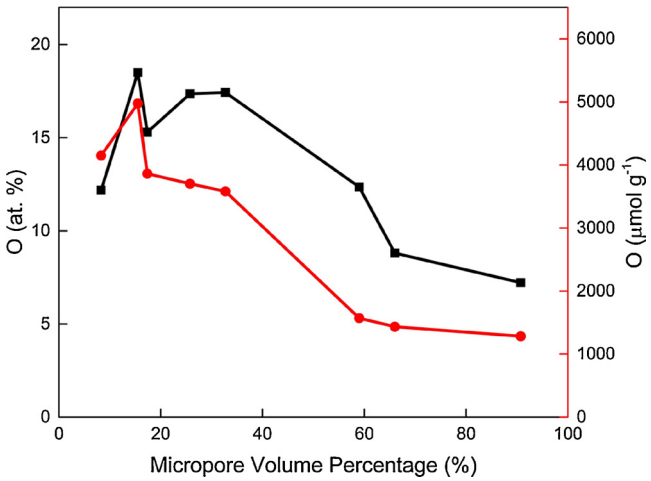

Fig. 3. Oxygen content inferred from TPD (red line) and XPS (black line) analyses as a function of micropore contribution to the structure of activated carbon materials. A similar trend by both techniques is clearly observed.

3.2. Electrochemical performance

It is well established that the surface oxygen groups increase the resistivity of carbon materials in which they increase the barrier for electron transfer from one microcrystalline carbon element to the other [36]. However, the conductivity values also depend on the porosity and surface-area values [37]. The presence of hierarchical porous networks enhances the movement of electrons from one microcrystalline to another and therefore induce the conductivity of the carbons. The conductivity of the KOH-*n* activated electrodes showed a correlation with the oxygen content, total pore volume and pore size distribution (Fig. S6). It was found that KOH − 0 sample with the limited microporosity had a conductivity value of 0.03 S cm^{-1}, that increased dramatically upon increasing the KOH loading content. KOH − 0.5 and KOH − 1 samples recorded values of 3.8 S cm^{-1} and 5 S cm^{-1}, similar to the values obtained for these activated carbons [38,39]. These observations confirm that different factors play a role in determining the resistivity of the carbon materials, and a balance between the porosity, pore size distribution and oxygen surface functionalities of carbons is needed to achieve optimized conductivity and thus electrochemical performance rates [40]. These results are further complemented with EIS measurements that allow the evaluation of the charge transfer resistance and electrolyte resistances inside the porous matrix [41]. The values of charge transfer resistance, governing the Faradaic processes, can be depicted from the depressed semicircle of the impedance Nyquist plots (Fig. S7) [42]. It was found that almost all samples do not reveal a clear semicircle, indicating insignificant charge transfer resistances due to limited redox reactions on the electrode surface. The values slightly decrease when the KOH/cellulose ratio is increased to 0.5:1 and 1:1. In addition, the impedance magnitude associated with the resistances of electrolyte ions inside the porous matrix at lowest frequency, decrease to a minimum in KOH − 0.1, KOH − 0.5 and KOH − 1 carbons. These results are attributed to the hierarchical porous structures with increased electrode surface area that enhance the electrolyte accessibility into the pores, despite the increase in oxygen functional groups. A detailed analysis of the impedance spectra of the activated carbons can be found elsewhere [43].

The electrochemical characterization of all carbon samples was obtained by applying a CV at a sweep rate of 5 mV s^{-1}. The voltammograms of all samples show a quasi-rectangular shape in the voltage range of -0.9 − 0.1 V, typical behaviour for EDLCs (Fig. 4, S8 and S9). However, for the low activated samples (KOH − 0, KOH − 0.005, KOH − 0.05, KOH − 0.1), the voltammetric charge is smaller at higher potentials compared to higher activated samples, indicating the hindrance of the ions in the ultra-porous structures. The KOH − 3 sample shows similar performance to the low-activated samples, which can be attributed to the drastic decrease in the total pore volume and decrease in the specific surface area upon extreme activation conditions. Moreover, this behaviour could be associated with a decrease in the electrical conductivity of the samples, as previously shown. These results are corroborated by the cyclic charge-discharge behaviour detected for all samples and shown in Fig. S10. The electrochemical performance of the carbons was enhanced upon increasing the KOH loading; the poor performance of the non-activated sample (KOH − 0) is attributed to the low specific surface area and very narrow microporosity. Upon increasing the KOH/cellulose ratio, the specific capacitance increases to 161 F g^{-1} for KOH − 0.5 and KOH − 1 samples and 0.5 A g^{-1} current density, owing to the hierarchical porous morphology and relatively high specific surface areas. In addition, a capacitance retention of 78% at 20 A g^{-1} current density is achieved in KOH − 1 sample, compared to 18% in the non-activated sample and 48% for KOH − 3 sample. The ohmic drop (iR), inferred from the discharge curve, also reflects the conductivity of the different samples, whereby the most conductive samples (KOH − 0.5 and KOH − 1) established the lowest iR drop, compared to the non-activated sample or the highest activated one. These results confirm that the accessibility of the electrolyte ions into the pores, at low and high current densities plays a major role in the electrochemical performance of the porous carbons. Specifically, an optimized electrode porous network for supercapacitor applications should be composed of i) micro- and mesopores that improve the charge storage mechanism and ii) macropores that facilitate the ion transport of the electrolyte at the electrode surface [44].

When the negative cut-off potential is extended towards more cathodic conditions to more negative values for all samples, a reduction current is generated at ~ -1.3 V, corresponding to the decomposition of water and nascent hydrogen evolution and its adsorption to the carbon electrodes. It should be noted that this reduction current is lower than the theoretical value of the equilibrium potential in 6 M KOH solution which is -0.872 V *vs.* standard hydrogen electrode (SHE) and hence -1.077 *vs.* the conventionally used Ag/AgCl reference electrode [45]. As this reduction occurs at voltages below -1.3 V *vs.* Ag/AgCl, an oxidation current of the hydrogen is present during the anodic scan at potentials around -0.7 V for low activated samples (KOH − 0, KOH − 0.005, and KOH − 0.01). This indicates that the hydrogen is weakly chemisorbed during the negative scan at lowest potential conditions in the low activated samples [14]. The noticeable hump due to the hydrogen oxidation starts broadening as the activation level further increases in KOH − 0.1 and KOH − 0.5 samples, and reappears once the activation level is further increased in the KOH − 1 and KOH − 2 samples. This is clearly illustrated upon extending the cut-off potential value to -1.5 V (Fig. 5). This behaviour is attributed to two main factors: i) the variation of the pore size distribution and contribution of ultra-micropores to the morphology of the carbons analysed by N_2 and CO_2 isotherms and MIP [10] and ii) the oxygen content in the different materials as detected by TPD, and XPS techniques [12]. The lowest activated carbons show the largest contribution of ultra-micropores in their structure; these micropores have proven to be effective for hydrogen adsorption and trapping [46]. In addition, these samples recorded the lowest oxygen content and thereby they constitute unsaturated sites in the porous structure, readily reactive in alkaline media at extreme cathodic conditions. However, the small anodic humps recorded for these samples are attributed to irreversible trapping of hydrogen in these structures. As for KOH − 1 and KOH − 2 samples, the high oxygen content offering less unsaturated sites for water reduction and interaction with nascent hydrogen, is mitigated by the fact that the oxygenated groups are associated with the hydrophilic surface functionalities that increase the wettability of the carbons and hence permit an easier admittance of the atoms / ions into the narrowest pores [18]. Furthermore, and despite the decrease in the total pore volume detected by CO_2 adsorption isotherms, the total ultra-microporous volume has drastically increased in these samples, in which the high specific surface area generates more active sites for the formation of hydrogen and its chemisorption to the carbon materials. The process can also be enhanced by the meso- and macroporous networks in these samples that ease the transport of the atoms/ions into the smaller pores [10]. These results confirm that there is not only one factor that dictates the hydrogen chemisorption mechanism and stability of porous carbon materials for electrochemical conversion and storage applications, but rather a balance between the chemistry and the porous texture.

The evaluation of the ratios of the cathodic current (I_{ca}) to anodic current (I_{an}) at an extreme cathodic condition of -1.3 V for the different carbon electrodes confirms that hydrogen evolution is less pronounced with i) increasing the oxygen content to an optimum along with ii) creating a hierarchical porous morphology in the carbon structure (Fig. 6). The decrease in the ratio of the current leap at extreme negative potentials to the nominal current range with increasing the KOH loading proves that the evolution of nascent hydrogen is more pronounced with low total pore volumes of dominant microporous morphology and small proportion of surface oxygen functionalities. The data point that does not follow the trend in Fig. 6b corresponds to KOH-3 sample that was characterized with sudden decrease in the specific surface area and total pore volume as previously mentioned. These

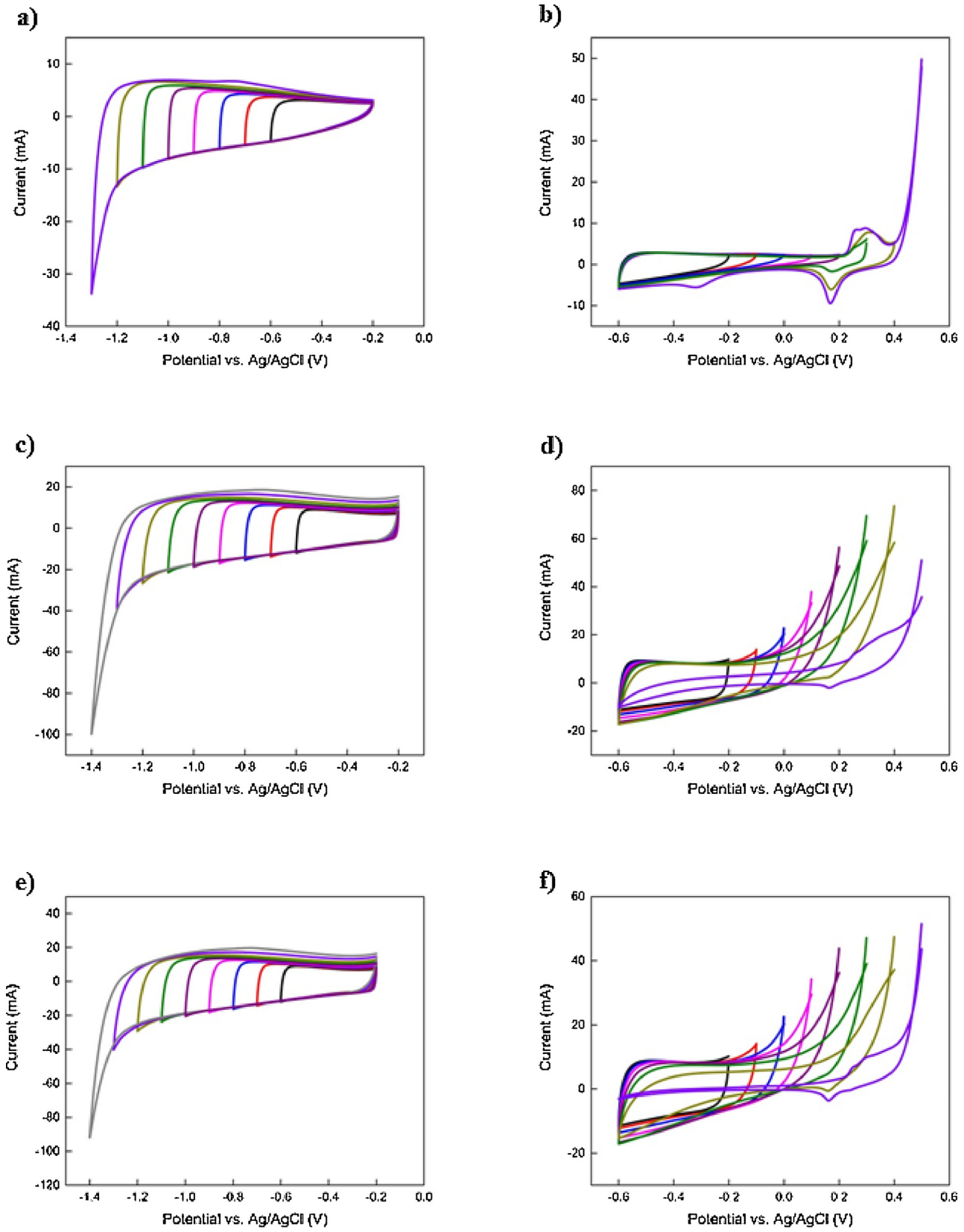

Fig. 4. Cyclic voltammograms of a) and b) KOH − 0, c) and d) KOH − 1 and e) and f) KOH − 2 at different potential ranges towards hydrogen evolution reaction (right) and oxygen evolution reaction (left).

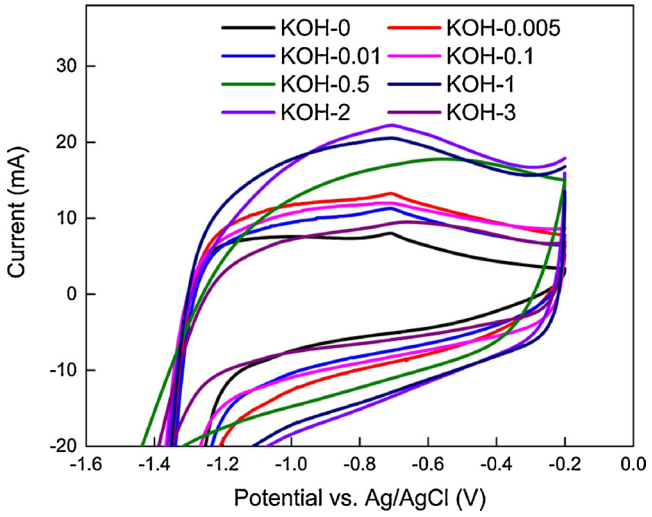

Fig. 5. Cyclic voltammograms of all activated carbons at a negative cut-off potential of -1.5 V and a scan rate of 5 mV s^{-1}.

observations establish that there is not one factor that determines the optimum performance of carbon electrodes; it is rather the co-dependence of various parameters that embellish a superlative electrochemical cell.

If the potential window is extended beyond -1.3 V to more negative values, the hydrogen oxidation hump during the positive scan increases, indicating higher amounts of chemisorbed hydrogen during the negative scan (Fig. S11). The decrease in the negative cut-off potential value, in the case of both KOH − 0 and KOH − 1 samples, increases the anodic peak of hydrogen oxidation and hence a more positive current and a more visible hump are recorded. In addition, the hump slightly shifts towards more positive values of potential as the negative potential window is further extended. At extreme cut-off potentials (as low as -2 V), the hydrogen is more strongly adsorbed to the porous carbon structure [16]. This implies that the different carbon electrodes possess the ability to store hydrogen in energetically different sites and that lower negative cut-off potential values reached, the higher the energy values of adsorption sites [11].

Upon expanding the potential window to more anodic conditions at more positive currents, an oxidation peak is evident at a voltage ~0.3 − 0.35 V in the CVs of low activated samples. A reduction peak occurs at ~ 0.2 V and -0.3 V during the cathodic scan in KOH − 0 and at ~ 0.2 V for all other activated carbons, which could be related to the reduction of the samples. The oxidation of the low activated samples exhibit a clear oxidation peak during the positive scan and the reverse processes did not occur at the same potential. This is attributed to the oxidation of the surface functionalities that are initially present in these samples, and further introduction of oxygen-containing functional groups when overcharging the electrode materials [22]. Hence, the electroactive redox species are introduced during the voltammetric cycles when the positive cut-off potential is extended to 0.4 V and 0.5 V with noticeable oxidation and reduction peaks. This indicates an increase in the surface oxygen groups during the positive scan that cannot be completely reversibly reduced during the cathodic scan. For the higher activated samples, KOH − 0.1, KOH − 1, KOH − 2 and KOH − 3, the oxidation reaction process occurs when the potential window is extended beyond 0.3 V, and a small hump is observed at 0.2 V during the negative scan. However, a clear but broad hump during the cathodic scan around a voltage of ~ 0.35 − 0.4 V is observed when the applied potential was extended towards 0.4 V and 0.5 V, with an irreversible reduction peak occurring during the negative scan. This could be attributed to the presence of a high oxygen content in the samples before electro-oxidation of water in an alkaline medium. The introduction of redox pairs in the high activated carbons have restricted electrochemical reactivity compared to the primary functionalities already present in the structure and hence smaller reduction peaks are observed in these samples due to high irreversibility [47]. It is worth mentioning that the nickel foam used as the current collector possess a similar trend at very positive/negative cut-off potentials; yet, the current values recorded are very low, and hence the nickel had an insignificant contribution to the electrochemical behaviour of the different activated samples (Fig. S12).

3.3. *In situ* Raman spectroscopy characterization

In situ Raman spectroscopy was employed to gain a better understanding of the mechanism of the hydrogen evolution and adsorption mechanisms in the porous carbons. This technique allows the structural characterization of carbon materials at different potentials and identifies changes at the carbon surfaces upon their electrochemical oxidation or reduction. The potentials applied to collect the Raman spectra was done following chronoamperometry to ensure stable potentials and was based on the potentials previously used in cyclic voltammetry experiments. A spectrum was first collected at -0.5 V and was further decreased to more negative potentials where electrochemical reduction occurs and then returning to more positive potentials. Fig. 7 and S13 present the Raman spectra of the different activated carbons recorded in three-electrode systems in 6 M KOH.

The D (~1330 cm^{-1}) and G (~1580 cm^{-1}) bands are observed in

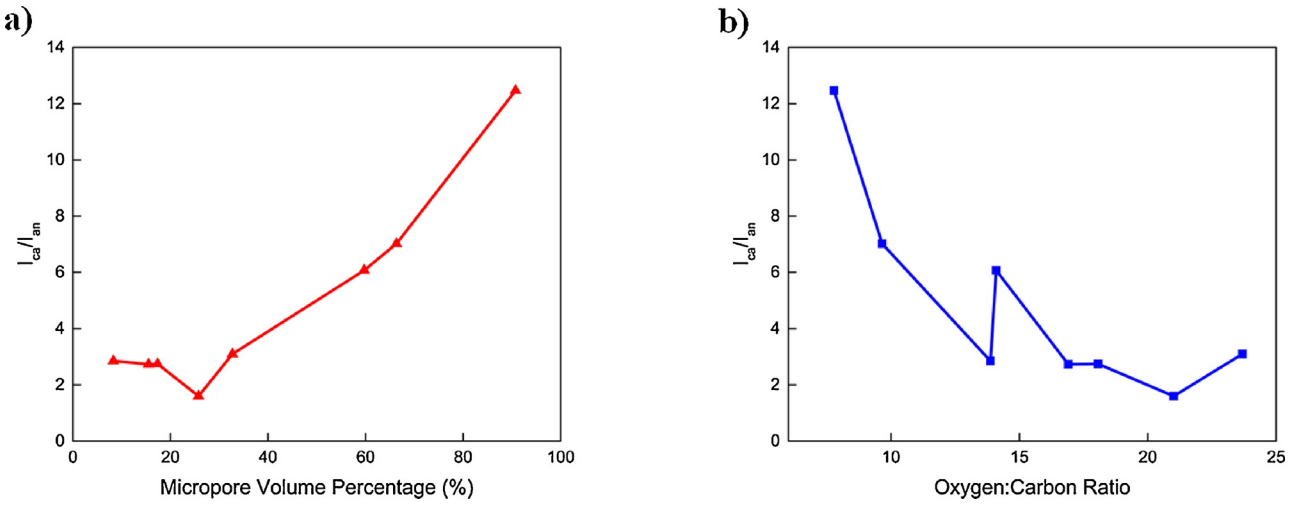

Fig. 6. I_{ca}/I_{an} ratio at extreme cathodic conditions of -1.3 V of the different activated samples with a) micropore volume contribution and b) oxygen content.

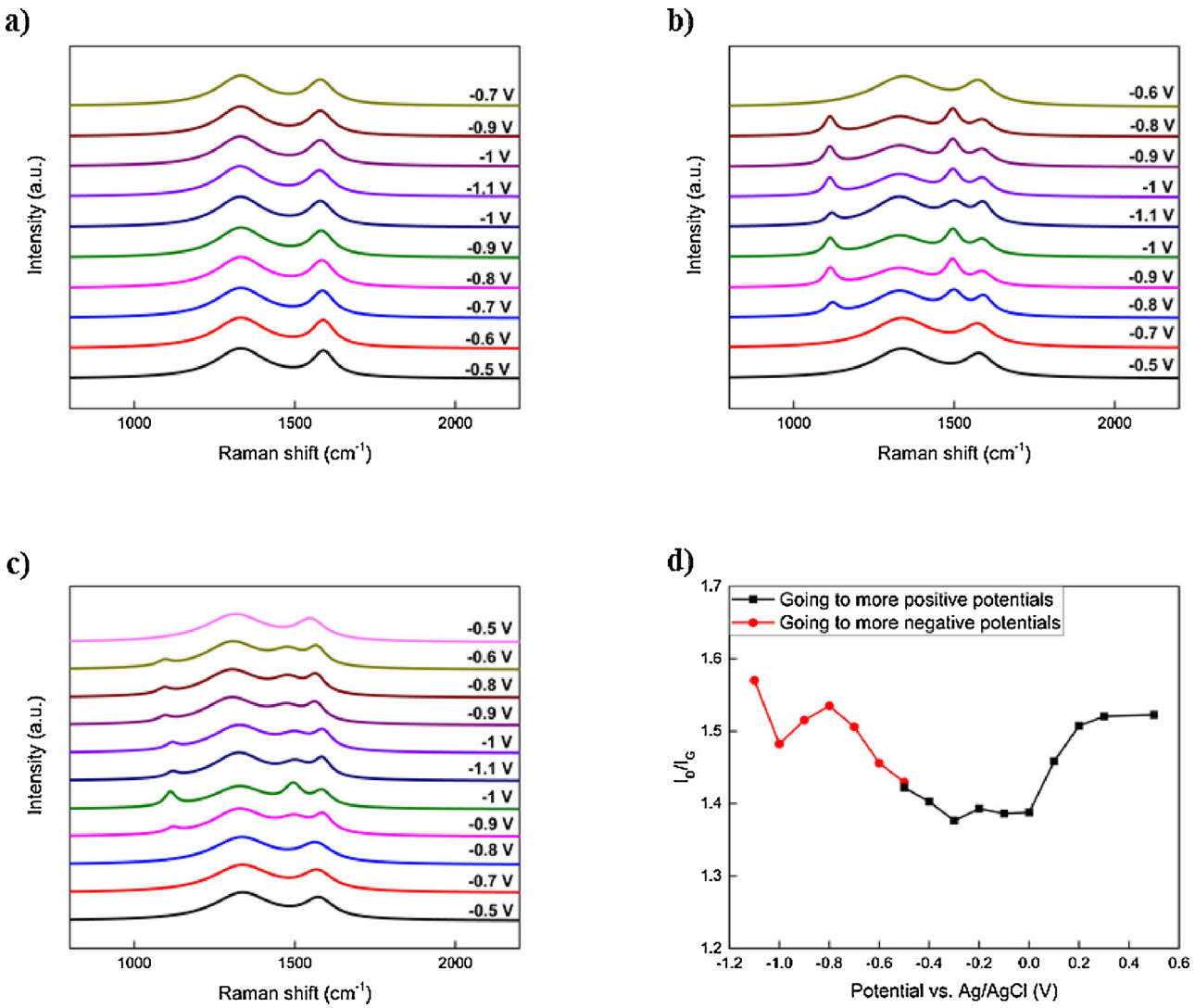

Fig. 7. Raman spectra for samples a) KOH − 0, b) KOH − 1 and c) KOH − 2 at different potentials in 6 M KOH and d) I_D/I_G for He-Ne laser of the KOH − 1 sample.

all experiments, a characteristic of graphene-based carbons. The D-band corresponds to the presence of defects in the carbon structure, and the G-band is related to the graphitic lattice vibration mode [48]. Upon decreasing the potential, different spectra were obtained in different porous carbon samples. KOH − 0 spectra reveal that the D-band's shift is insignificant, while the G-band position was shifted by almost 10 Raman shifts in the positive direction upon decreasing the potential to -1.1 V. This can be attributed to a change in the hydrogen content in the carbon bulk and/or a slight change in the sp^2 domain size [49]. In addition, both bands have broadened upon decreasing the applied potential, illustrating that a higher degree-of-disorder is introduced into the structure upon applying extreme potentials [50]. This is also confirmed with the increase of relative intensity ratio of the D-band (I_D) to the G-band (I_G) (Fig. S14). Applying potentials more negative than -1.1 V to this sample caused the evolution of hydrogen bubbles and hence the contact with the current collector is lost and the spectra cannot be recorded. The hydrogen evolution occurred in these samples as indicated by CV and *in situ* Raman spectroscopy experiments, yet the chemisorption of the hydrogen gas was too weak to be recorded before the bubbling process. This is attributed to two factors: i) the narrow microporous morphology in these samples, which enhances the hydrogen chemisorption and trapping in the ultra-porous structures, and ii) low oxygen content, that impedes the electrolyte wettability on the carbon surfaces. Similar behaviour was recorded for KOH − 0.005, KOH − 0.01 and KOH − 0.1 samples. Hence, the hydrogen gas evolution in these samples, as shown in the CV curves, is detected before recording the hydrogen chemisorption, regardless of the facile formation of the weak carbon-hydrogen bonds in unsaturated sites in the carbon bulk.

When the KOH activation ratio was further increased, a different behaviour was observed. Decreasing the applied potential introduced two bands at ~ 1110 cm^{-1} (D4) and 1500 cm^{-1} (D3), which both correspond to the electrochemical hydrogen storage, and are assigned to C(sp^2)-H and C=C stretching vibrations, respectively [51]. This suggests that the bands observed are a consequence of the formation of carbon-hydrogen bonds and a structural change on the carbon surface occurs when the potential is decreased to -0.8 V in KOH − 0.5 and KOH − 1 samples, and at -0.9 V for KOH − 2 and KOH − 3 samples. The D and G bands are both narrowed upon the introduction of D3 and D4 bands, which have been suggested previously as a direct consequence of the hydrogenation of carbon [12]. The bands appear and disappear simultaneously, which indicates the reversibility of hydrogen chemisorption. However, these bands appear at -0.8 V for KOH − 1 sample and at -0.9 V for KOH − 2 sample, showing that hydrogenation is easier in the former sample. In addition, D3 and D4 bands disappear when increasing the potential for the different activated carbons. The potential corresponding to complete reversibility of the hydrogen reduction is -0.2 V for KOH − 0.5, -0.6 V for KOH − 1 and -0.5 V for KOH − 2 sample. This is due to the different trends obtained in total pore

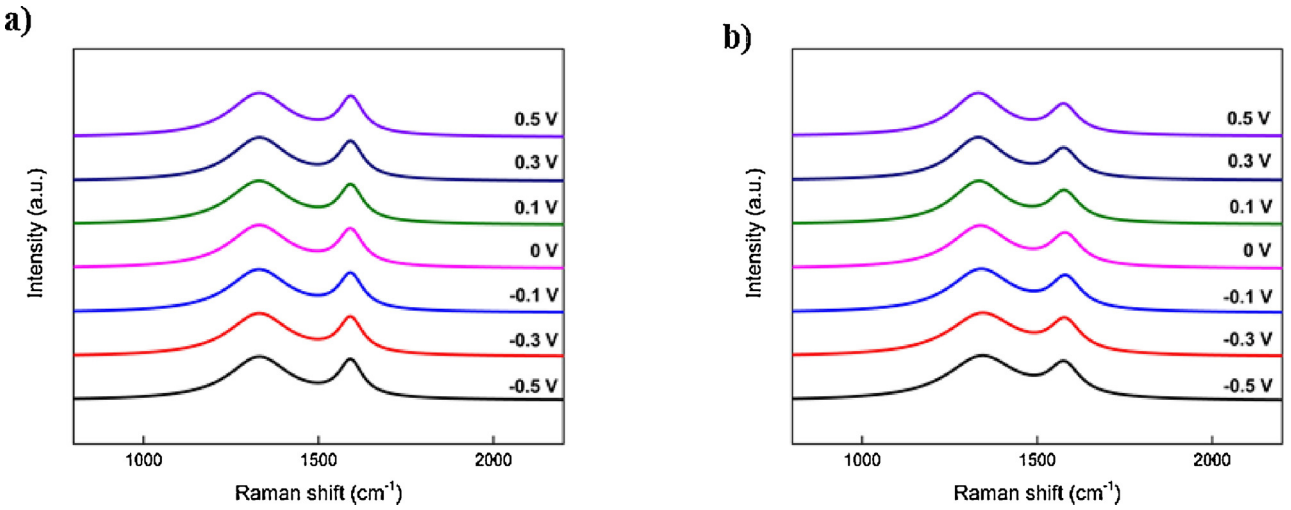

Fig. 8. Raman spectra for a) KOH − 0 and b) KOH − 1 samples at different potentials going to more positive potentials.

volume, specific surface area and oxygen content, in which the increase in oxygen surface functionalities, along with the specific surface area and wide pore size distribution, does not only enhance the adsorption of hydrogen onto the porous media, but also improves the reversibility of the reduction reaction that occurs at negative potentials. The different oxygen functionalities enhance the wettability of the ultra-microporous carbons and therefore the chemisorption of the hydrogen to the carbons. The increase in pore volume improves the transport of the hydrogen ions/atoms in and out of the porous networks and permits more active sites for the nascent hydrogen [11]. These results highlight that the presence of free active sites and decreasing the number of dangling atoms on the carbon is not the only factor that affects the hydrogen chemisorption mechanism. Specifically, at high scan rates, the electrode material would not have the sufficient time for the carbon hydrogenation mechanism and hence evolution of hydrogen gas would occur first. This would impede the capacitive mechanism and deteriorate the electrochemical performance. On the other hand, and despite the fact the higher KOH-activated samples consisted of high amounts of oxygenated groups, the hierarchical porous network structure enhanced the hydrogenation mechanism and extending the potential window, with avoiding the evolution of nascent hydrogen. All of the aforementioned factors are deduced to affect the rate of hydrogenation of the carbon atoms and finding the right configuration and balance between all key factors plays an important role in optimizing the porous carbons for the required application. This proves that the understanding the interrelationship between the porous structure, oxygen content and the highest possible applied potentials is necessary to prevent hydrogen evolution for supercapacitor devices at extreme conditions.

The I_D/I_G ratio (Fig. 7d and S13) followed a similar trend in all high activated samples upon decreasing the potential, whereby the degree-of-disorder in the graphitic structure increased once the carbon-hydrogen bonds formed at -0.8 V or -0.9 V for different samples, and then decreased upon further decrease in the potential. This could be attributed to the introduction of the D3 and D4 bands when carbon hydrogenation occurs, whereby the intensity and the width of the first order D-band decrease, hence decreasing the I_D/I_G ratio. The position of both first-order bands shift by almost 10 Raman shifts, the D-band to lower frequency, and that of G-band to a higher frequency, confirming the transition from a graphitic to more amorphous carbon [52].

Going to more positive potentials starting from -0.5 V, no changes in the bands have been observed in the low activated carbons (Fig. 8a). On the contrary, the recorded spectra show very similar behaviour to that obtained when the electrodes were negatively polarized before going to more positive potentials. This confirms that applying potentials close to the electrolysis of water would not affect the surface chemistry of these carbons and hence their durability is promising as electrode materials for supercapacitor devices. The width of both first-order bands and their respective positions insignificantly changed upon increasing the positive cut-off potential to 0.5 V. The ratio between the D and G band intensities (I_D/I_G) stays almost constant with the electrochemical processes (Fig. 7d and S15). This indicates that the electrochemical oxidation treatment does not degrade these samples and the degree-of-disorder of the graphitic structure stays constant, and hence the carbon surface is not modified. This can be attributed to the porous structure that is dominated by ultra-micropores in the samples and hence the evolution of oxygen, and as detected by the CV curves, cannot reach the smallest pores and the number of unsaturated active sites in these samples within the short Raman spectra scan (Fig. 8b). As for the higher activated samples, the D-band and G-band widths decreased by almost 25% and 10%, respectively, and the D-band was shifted to lower frequencies when the potential was increased. The intensity ratio between both bands (I_D/I_G) also increased when the potential window was extended beyond 0 V, confirming the modification in the carbon structure and an increase in the degree-of-disorder of these carbons. The initial composition of these samples with high oxygen content, hence Faradaic contribution, as previously shown, might have had a contribution in the oxygen evolution at these potentials. In addition, the meso- and macropores ease the transport of the oxygen ions/atoms into the carbon bulk, which modifies the surface chemistry of the materials.

Upon evaluating the I_{an}/I_{ca} ratio at an extreme anodic condition of 0.5 V from the CV profiles obtained in the previous section, it is illustrated that the oxygen content and total microporous contribution hugely affect the progress of the oxygen gas evolution process. Despite the fact that the evolution of oxygen is more pronounced in the low-activated samples demonstrated with high current jumps at extreme positive potentials (Fig. S15), the modification of the carbon electrodes occurred only at high KOH loadings (with higher oxygen content and total pore volumes) at cathodic conditions, as detected by Raman spectra. These results thus emphasize the necessity of complementing surface science and electrochemical techniques so as to optimize the balance between different parameters that play a key role in determining the stability of the carbon electrodes at extreme potentials.

4. Conclusions

Porous carbons with different pore structures and surface chemistries have been investigated to identify the effect of oxygenated functional groups on their performance as supercapacitor electrode materials. The combination of chemical and electrochemical characterization methods was used to determine the electrochemical

surface properties of KOH − activated carbons. *In situ* Raman spectroscopy, XPS and TPD coupled with mass spectrometry confirmed that the increase in oxygen surface functionalities, together with a sufficiently wide porosity, allow an easy wettability of electrodes and hence reversible hydrogen chemisorption. The hydrogenation of carbon atoms can hence be delayed to occur, highlighting the importance of surface chemistry and porous texture of the carbon materials. The reversible hydrogen oxidation process is further delayed at high activation conditions due to the combination of high oxygen content and ultra-microporous structures which give rise to strong hydrogen adsorption and trapping in the porous media and hydrogen storage at energetically different carbon sites. The results show that most of the active sites for hydrogen chemisorption are located in the microporosity and if it is not accessible by the electrolyte, no hydrogen storage occurs. Hence the importance of meso- and macro-porous structures in delaying the water electrolysis process. Furthermore, the extreme anodic and cathodic conditions modified the surface chemistry of the carbons at different conditions, which indicates that all factors that affect the hydrogenation of carbon and its stability at extreme electrochemical conditions have to be considered for optimized processes in supercapacitor applications.

Acknowledgements

The authors wouldlike to thank the Engineering and Physical Sciences Research (EPSRC) for financial support of electrochemical energy conversion and storage research in the Electrochemical Innovation Lab (EP/R023581/1; EP/P009050/1; EP/N032888/1; EP/K014706/2; EP/M014371/1; EP/M023508/1; EP/M009394/1; EP/K038656/1), the Royal Academy of Engineering, Generalitat Valenciana and FEDER (PROMETEOII/2014/010), projects CTQ2015-66080-R (MINECO/FEDER). M.M.T and D.I.A. are grateful to UPM-Kymmene Corporation that provided the cellulose materials used throughout the experiments. M.J.M.L. acknowledges Generalitat Valenciana for the financial support through a VALi + d contract (ACIF/2015/374). I.P.P and G.H. thank the China Scholarship Council (CSC) and EPSRC for their financial support (EP/L015862/1).

Appendix A. Supplementary data

Supplementary material related to this article can be found, in the online version, at doi:https://doi.org/10.1016/j.est.2018.08.014.

References

[1] E. Frackowiak, F. Béguin, Carbon 40 (2002) 1775–1787.
[2] M. Sevilla, R. Mokaya, Energy Environ. Sci. 7 (2014) 1250–1280.
[3] M. Pumera, Energy Environ. Sci. 4 (2011) 668–674.
[4] H. Wang, Q. Gao, J. Hu, J. Am. Chem. Soc. 131 (2009) 7016–7022.
[5] J. Gamby, P.L. Taberna, P. Simon, J.F. Fauvarque, M. Chesneau, J. Power Sources 101 (2001) 109–116.
[6] A. Balducci, R. Dugas, P.L. Taberna, P. Simon, D. Plée, M. Mastragostino, S. Passerini, J. Power Sources 165 (2007) 922–927.
[7] Y. Zhu, S. Murali, M.D. Stoller, K.J. Ganesh, W. Cai, P.J. Ferreira, A. Pirkle, R.M. Wallace, K.A. Cychosz, M. Thommes, D. Su, E.A. Stach, R.S. Ruoff, Science 332 (2011) 1537–1541.
[8] M.A. de la Casa-Lillo, F. Lamari-Darkrim, D. Cazorla-Amorós, A. Linares-Solano, J. Phys. Chem. B 106 (2002) 10930–10934.
[9] K. Jurewicz, E. Frackowiak, F. Béguin, Electrochem. Solid-state Lett. 4 (2001) A27–A29.
[10] F. Béguin, M. Friebe, K. Jurewicz, C. Vix-Guterl, J. Dentzer, E. Frackowiak, Carbon 44 (2006) 2392–2398.
[11] F. Béguin, K. Kierzek, M. Friebe, A. Jankowska, J. Machnikowski, K. Jurewicz, E. Frackowiak, Electrochim. Acta 51 (2006) 2161–2167.
[12] M.J. Bleda-Martínez, J.M. Pérez, A. Linares-Solano, E. Morallón, D. Cazorla-Amorós, Carbon 46 (2008) 1053–1059.
[13] B. Fang, H. Zhou, I. Honma, J. Phys. Chem. B 110 (2006) 4875–4880.
[14] S. Leyva-García, E. Morallón, D. Cazorla-Amorós, F. Béguin, D. Lozano-Castelló, Carbon 69 (2014) 401–408.
[15] K. Jurewicz, E. Frackowiak, F. Béguin, Fuel Process. Technol. 77-78 (2002) 415–421.
[16] K. Jurewicz, E. Frackowiak, F. Béguin, Appl. Phys. A 78 (2004) 981–987.
[17] C. Portet, P.L. Taberna, P. Simon, E. Flahaut, C. Laberty-Robert, Electrochim. Acta 50 (2005) 4174–4181.
[18] B.E. Conway, Electrochemical Supercapacitors: Scientific Fundamentals and Technological Applications, Springer Science & Business Media, 2013.
[19] Y. Zhai, Y. Dou, D. Zhao, P.F. Fulvio, R.T. Mayes, S. Dai, Adv. Mater. 23 (2011) 4828–4850.
[20] K. Kinoshita, J. Bett, Carbon 11 (1973) 403–411.
[21] K. Kinoshita, J.A.S. Bett, Carbon 13 (1975) 405–409.
[22] K. Kinoshita, (1988).
[23] C. Kozlowski, P.M. Sherwood, J. Chem. Soc. Faraday Trans.: Phys. Chem. Condensed Phases 80 (1984) 2099–2107.
[24] D.I. Abouelamaiem, G. He, I. Parkin, T.P. Neville, A.B. Jorge, S. Ji, R. Wang, M.-M. Titirici, P.R. Shearing, D.J.L. Brett, Sustain. Energy Fuels (2018).
[25] Z. Ryu, J. Zheng, M. Wang, Carbon 36 (1998) 427–432.
[26] Z. Ryu, J. Zheng, M. Wang, B. Zhang, Carbon 37 (1999) 1257–1264.
[27] R. Gómez, J.M. Pérez, J. Solla-Gullón, V. Montiel, A. Aldaz, J. Phys. Chem. B 108 (2004) 9943–9949.
[28] G. Kister, G. Cassanas, M. Vert, Polymer 39 (1998) 267–273.
[29] S. Leyva-García, K. Nueangnoraj, D. Lozano-Castelló, H. Nishihara, T. Kyotani, E. Morallón, D. Cazorla-Amorós, Carbon 89 (2015) 63–73.
[30] M.J. Mostazo-López, R. Ruiz-Rosas, E. Morallón, D. Cazorla-Amorós, Carbon 91 (2015) 252–265.
[31] C.A. León y León, Adv. Colloid Interface Sci. 76-77 (1998) 341–372.
[32] D. Enke, F. Janowski, W. Schwieger, Microporous Mesoporous Mater. 60 (2003) 19–30.
[33] M.J. Bleda-Martínez, D. Lozano-Castelló, E. Morallón, D. Cazorla-Amorós, A. Linares-Solano, Carbon 44 (2006) 2642–2651.
[34] F. Rodrıguez-Reinoso, M. Molina-Sabio, Adv. Colloid Interface Sci. 76 (1998) 271–294.
[35] J. Figueiredo, M. Pereira, M. Freitas, J. Orfao, carbon 37 (1999) 1379–1389.
[36] M. Polovina, B. Babić, B. Kaluderović, A. Dekanski, Carbon 35 (1997) 1047–1052.
[37] A.G. Pandolfo, A.F. Hollenkamp, J. Power Sources 157 (2006) 11–27.
[38] M. Olivares-Marín, J.A. Fernández, M.J. Lázaro, C. Fernández-González, A. Macías-García, V. Gómez-Serrano, F. Stoeckli, T.A. Centeno, Mater. Chem. Phys. 114 (2009) 323–327.
[39] M. Sevilla, G.A. Ferrero, A.B. Fuertes, Carbon 114 (2017) 50–58.
[40] B. Xu, F. Wu, Y. Su, G. Cao, S. Chen, Z. Zhou, Y. Yang, Electrochim. Acta 53 (2008) 7730–7735.
[41] S. Fletcher, V.J. Black, I. Kirkpatrick, J. Solid State Electrochem. 18 (2014) 1377–1387.
[42] J. Yan, Z. Fan, T. Wei, W. Qian, M. Zhang, F. Wei, Carbon 48 (2010) 3825–3833.
[43] D.I. Abouelamaiem, G. He, T.P. Neville, D. Patel, S. Ji, R. Wang, I.P. Parkin, A.B. Jorge, M.-M. Titirici, P.R. Shearing, D.J.L. Brett, Electrochim. Acta 284 (2018) 597–608.
[44] D.-W. Wang, F. Li, M. Liu, G.Q. Lu, H.-M. Cheng, Angew. Chemie Int. Ed. 47 (2008) 373–376.
[45] C. Vix-Guterl, E. Frackowiak, K. Jurewicz, M. Friebe, J. Parmentier, F. Béguin, Carbon 43 (2005) 1293–1302.
[46] M. Rzepka, P. Lamp, M.A. de la Casa-Lillo, J. Phys. Chem. B 102 (1998) 10894–10898.
[47] M.P. Bichat, E. Raymundo-Piñero, F. Béguin, Carbon 48 (2010) 4351–4361.
[48] F. Tuinstra, J.L. Koenig, J. Chem. Phys. 53 (1970) 1126–1130.
[49] J.H. Kaufman, S. Metin, D.D. Saperstein, Phys. Rev. B 39 (1989) 13053–13060.
[50] K.N. Kudin, B. Ozbas, H.C. Schniepp, R.K. Prud'homme, I.A. Aksay, R. Car, Nano Lett. 8 (2008) 36–41.
[51] H. Kuzmany, R. Pfeiffer, N. Salk, B. Günther, Carbon 42 (2004) 911–917.
[52] A.C. Ferrari, J. Robertson, Phys. Rev. B 61 (2000) 14095–14107.